THE JOURNAL OF
PHYSICAL CHEMISTRY C

pubs.acs.org/JPCC

Article

Differentiating the Electrical and Optoelectrical Properties of Oxysulfides $La_2Ta_2MS_2O_8$ (M = Zr, Ti) via Application of Pressure

Junxiu Liu, Jian Chen, Weiwei Li, Hua Tian, Xiaoliang Zhang, Nana Li, Jinyuan Yan, Martin Kunz, Bin Chen, and Hengzhong Zhang*

Cite This: *J. Phys. Chem. C* 2020, 124, 14477−14484

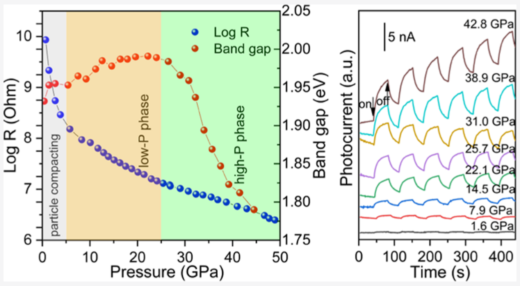

ABSTRACT: The oxysulfides $La_2Ta_2MS_2O_8$ (M = Zr, Ti) form a new family of narrow-band-gap semiconductors that have a lot of potential for photocatalysis and optoelectronics. However, many of their fundamental properties are still unknown. Herein, we report their crystal structure evolution, electrical resistances, band gaps, and photocurrents under compression from near ambient pressure up to ∼50 GPa. Our results show that the orthorhombic phases of $La_2Ta_2ZrS_2O_8$ and $La_2Ta_2TiS_2O_8$ transform into two new high-pressure phases at ∼23 and 25 GPa, respectively. Although their band gaps show similar trends in variations with the pressure, the resistance of $La_2Ta_2ZrS_2O_8$ is ∼2−3 orders of magnitudes higher than that of $La_2Ta_2TiS_2O_8$. In addition, the former exhibits a sharp decrease with pressure after the phase transition, while the latter presents only a steady decrease with increasing pressure. This difference arises from their different responses in the carrier mobility under compression, which is related to their compressibility at high pressure (the bulk modulus of $La_2Ta_2ZrS_2O_8$ is 122.5 GPa and that of $La_2Ta_2TiS_2O_8$ is 132.6 GPa). Both the electrical conductivity and defect formation at high pressure can affect the photoelectric properties, making the $La_2Ta_2TiS_2O_8$ compound possess photocurrents superior to the $La_2Ta_2ZrS_2O_8$ one. The findings from this work show that the $La_2Ta_2TiS_2O_8$ compound is a better candidate than $La_2Ta_2ZrS_2O_8$ for developing applications in photocatalysis, photovoltaics, photoelectric devices, etc.

1. INTRODUCTION

Technologies devoted to fabricating light-harvesting materials for solar conversion via photovoltaics or photocatalysis frequently involve applications of semiconductors. Unary (or simple) semiconductor transition-metal oxides containing Ti^{4+}, Zr^{4+}, Nb^{5+}, Ta^{5+}, etc., can function as photocatalysts for water splitting under the illumination of ultraviolet (UV) light.[1−3] Some Ti^{4+}-, Zr^{4+}-, Nb^{5+}-, and Ta^{5+}-based mixed (or complex) metal oxides[4−6] (such as $SrTiO_3$, $NaTaO_3$, and $K_2La_2Ti_3O_{10}$) have also been successfully used to produce water splitting under UV light. However, these metal oxides rarely absorb visible light because the tops of their valence bands consist of O 2p orbitals that lead to the formation of large band gaps in the semiconductors (>3 eV).[3,7] On the other hand, some metal chalcogenides (such as CdS and CdSe) have band gaps small enough to absorb visible light. However, the S^{2-} and Se^{2-} anions in these metal chalcogenides are susceptible to oxidation in water, making them unstable in photocatalysis. Combining the advantages of oxides in stability and sulfides in small band gaps, mixed transition-metal oxysulfides such as $Sm_2Ti_2S_2O_5$[8] and $La_2Nb_3S_2O_8$[9] are promising candidates for visible-light-driven photocatalysis. This is because in the valence bands of the oxysulfides, the more positive potentials of the S 3p orbitals compared to the O 2p orbitals shift the top of the valence band closer to the conduction bands and hence make the band gaps of the oxysulfides narrower than the ones of corresponding pure oxides.[10] In view of this, we studied in this work two novel oxysulfides, $La_2Ta_2ZrS_2O_8$ and $La_2Ta_2TiS_2O_8$,[10] aiming at obtaining fundamental knowledge about their electrical resistances that are essential for their photocatalytic applications. Like temperature, pressure can modulate the crystal structures and hence the properties of materials,[11] yet without changing the chemical compositions in most cases. Thus, in this work, we investigated the pressure-induced crystal structure evolution, electrical resistances, light absorption, and photocurrents of $La_2Ta_2ZrS_2O_8$ and $La_2Ta_2TiS_2O_8$ using high-pressure (HP) X-ray diffraction (XRD), Raman spectroscopy, UV−vis absorption spectroscopy, and electrical transport and optoelectrical measurements. The knowledge obtained from this work may provide a route directing to novel applications of the new oxysulfide materials.

Received: April 10, 2020
Revised: May 18, 2020
Published: May 22, 2020

https://dx.doi.org/10.1021/acs.jpcc.0c03231
J. Phys. Chem. C 2020, 124, 14477−14484

2. EXPERIMENTAL DETAILS

2.1. Synthesis and Characterization. The oxysulfides $La_2Ta_2ZrS_2O_8$ and $La_2Ta_2TiS_2O_8$ were synthesized from solid-state reactions based on a previously described procedure.[10] The required stoichiometries of La_2O_3 (Macklin, 99.99%), La_2S_3 (Alfa Aesar, 99.0%), Ta_2O_5 (Macklin, 99.99%), ZrO_2 (Macklin, 99.99%), or TiO_2 (Macklin, 99.9%), as well as some elemental S (99.99% in purity) for retarding oxide formation, were thoroughly ground and mixed in an agate mortar. The mixture was pressed to form a thin disk and then placed in a small and short quartz tube that had only one open terminal. The opening was sealed-off in a high-temperature gas flame, while the tube was under vacuum pumping (Partulab MRVS, Partulab Technology Co. Ltd). The sealed quartz tube was heated at 1100 °C for 72 h in an electric furnace, then quenched to room temperature by turning off the power. The cooled product was ground, resealed in a quartz tube, and then reheated, as described above. The grinding−reheating procedure was repeated 2−3 times, attempting to maximize the oxysulfide production.

X-ray diffraction analyses of the synthesized samples were performed using a Malvern Panalytical X-ray diffractometer with a Cu $K\alpha$ radiation (X-ray wavelength 1.54056 Å). The XRD patterns were taken in the 2θ range from 10 to 90° at ambient pressure and room temperature.

Ambient pressure UV−vis absorption spectra of the samples were measured using an Agilent Cary 5000 spectrophotometer at room temperature. The UV−vis spectra were collected from 300 to 800 nm in the wavelength with a poly(tetrafluoroethylene) integrating sphere attachment.

2.2. In Situ High-Pressure (HP) XRD and Raman Spectroscopy. The in situ HP-XRD measurements were performed at the synchrotron beamline 12.2.2 of the Advanced Light Source (ALS), Lawrence Berkeley Laboratory, with a beam energy of 25 keV (wavelength 0.4959 Å).[12] A symmetric diamond-anvil cell (DAC) with an anvil culet size of 300 μm was used to generate the required high pressures on a sample. A T301 stainless steel gasket was perforated through the center of the gasket during preindentation, forming a hole of ~130 μm acting as the sample chamber. Neon was used as the pressure-transmitting medium, and the sample pressure was measured using the ruby fluorescence method.[13] Rietveld analyses of the XRD data were conducted using the General Structure Analysis System (GSAS) program to identify the phases and refine the crystal structure parameters.[14]

For HP-Raman measurements, similar to the HP-XRD experiments, a sample was loaded into a DAC with Ne as the pressure-transmitting medium. Then, the HP-Raman spectra were collected with a Raman spectrometer (inVia Reflex, Renishaw) using a 532 nm excitation laser.

2.3. In Situ High-Pressure Electrical Resistance, Photocurrent, and UV−Vis Absorption Spectroscopy Measurements. High-pressure electrical resistance measurements were conducted in a diamond-anvil cell using a two-probe resistance test method. A T301 stainless steel gasket was preindented to 35 μm in thickness and a hole of 250 μm in diameter was drilled through the gasket center. A thin layer of cubic boron nitride (cBN) was inserted between the steel gasket and the diamond culet to insulate the electrical leads (platinum) from the metal gasket. Then, another hole with a diameter of 150 μm was drilled through the cBN center, serving as the sample chamber. The pressure of the loaded sample was determined using the ruby fluorescence method. No pressure-transmitting medium was used, preventing interferences to the electrical measurements. The alternating current (AC) impedance spectroscopy of the sample at high pressure was measured using an impedance analyzer (model CS353, Wuhan CorrTest Instr. Corp., Ltd., or Model Zahner Ennium, Zahner) in the frequency range of 0.01 Hz−10 MHz.

The same sample setup as that used in the resistance measurements was used for the photocurrent measurements of the sample at high pressure. A 10 W LED lamp with a wavelength ranging from 400 to 410 nm was used as the light source. The photocurrent was measured using a high-resistance meter (Keithley 6517B, A Tektronix Co., Ltd.) after applying a direct current (DC) voltage of 3 V on the sample. Then, a 40 s pulse of light was used to illuminate repeatedly on the sample under testing.

For the in situ high-pressure UV−vis absorption measurements of a sample loaded in a DAC, silicone oil was used as the pressure-transmitting medium. The spectra were collected using a custom-built UV−vis absorption spectrophotometer in the wavelength range from 400 to 800 nm with a response time of 3 s.

3. RESULTS AND DISCUSSION

3.1. Sample Characterization. Figure 1a,b shows XRD patterns of the synthesized $La_2Ta_2ZrS_2O_8$ sample (denoted "LTZSO sample" hereafter) and $La_2Ta_2TiS_2O_8$ sample (denoted "LTTSO sample" hereafter) at room temperature. Rietveld analyses of the XRD data show that most of the diffraction peaks of the LTZSO sample (Figure 1a) can be assigned to the $La_2Ta_2ZrS_2O_8$ compound, while the rest can be assigned to the oxide $LaTaO_4$. The $La_2Ta_2ZrS_2O_8$ compound has an orthorhombic structure (space group *Pnnm*; ICSD #252328[15]) with a content of 81.5 wt %, while the $LaTaO_4$ compound exists in both the orthorhombic structure (space group $Cmc2_1$; COD #1533637[16]) with a content of ~14.2 wt % and the monoclinic structure (space group $P2_1/c$; COD #1530210[16]) with a content of ~4.3 wt %. Rietveld analyses also show that the synthesized LTTSO sample consisted of the target $La_2Ta_2TiS_2O_8$ compound in the orthorhombic structure (space group *Pnnm*; ICSD #252329[15]) with a content of ~55.1 wt % and the oxide $LaTaTiO_6$ in an orthorhombic structure (*Pnma*, COD #9015033[16]) with a content of ~44.9 wt %. The lattice parameters of the oxysulfides obtained from the Rietveld analyses are listed in Table 1.

We were unable to produce single-phase oxysulfides as reported in the previous work[10] even after doing repeated grinding−sintering cycles. Perhaps the amount of the excess sulfur needs more careful adjustment, which was not realized and tested at the time of the sample syntheses. However, the contained oxides do not affect the measured electrical resistances and photocurrents of the samples because their band gaps are much higher than those of the oxysulfides (see below).

Figure 1c shows the UV−vis absorption spectra of the LTZSO and LTTSO samples at the ambient pressure. The absorption edge is ~530 nm for the LTZSO sample and ~680 nm for the LTTSO sample, corresponding to a band gap of 2.3 and 1.8 eV for orthorhombic $La_2Ta_2ZrS_2O_8$ and $La_2Ta_2TiS_2O_8$, respectively (see below). The band gap of $La_2Ta_2TiS_2O_8$ is narrower than that of $La_2Ta_2ZrS_2O_8$ due to the lower energy of the Ti 3d orbital compared to the Zr 4d orbital in the conduction bands.[10]

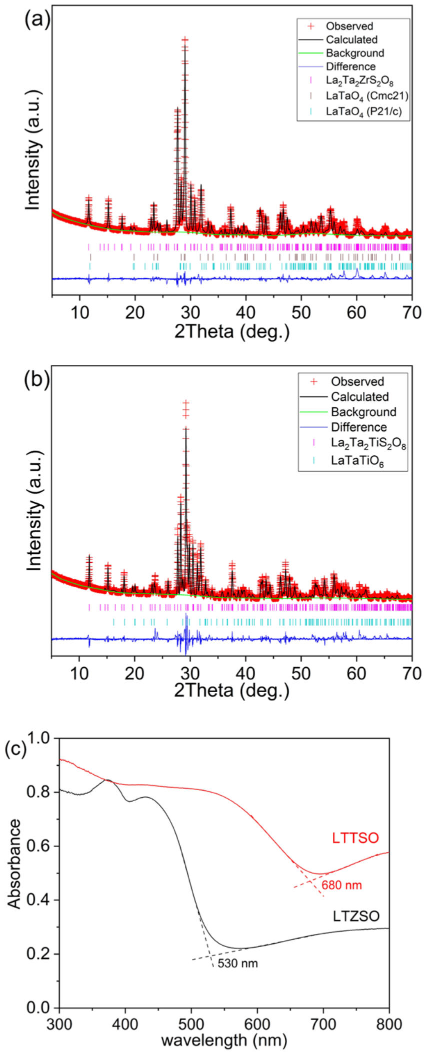

Figure 1. Ambient condition X-ray diffraction patterns (X-ray wavelength 1.54056 Å) and Rietveld fittings of the synthesized LTZSO (a) and LTTSO (b) samples and UV−vis spectra (c) of the two samples.

Table 1. Rietveld Refined Lattice Parameters of the Orthorhombic Phases of $La_2Ta_2ZrS_2O_8$ and $La_2Ta_2TiS_2O_8$ at Ambient Pressure

lattice parameters	*a* (Å)	*b* (Å)	*c* (Å)
$La_2Ta_2ZrS_2O_8$	10.0447(5)[a]	11.6730(7)	7.7654(3)
$La_2Ta_2TiS_2O_8$	9.8199(5)	11.6962(8)	7.6941(4)

[a]Denoting an estimated standard deviation of 0.0005 Å.

As the synthesized oxysulfide samples contained impurity products $LaTaO_4$ and $LaTaTiO_6$, we also synthesized chemically pure $LaTaO_4$ and $LaTaTiO_6$ (see the Supporting Information (SI)) to evaluate their contributions to the electrical properties of the two oxysulfide samples. The XRD patterns (Figure S1a) of the synthesized samples show that the $LaTaO_4$ sample is a mixture of an orthorhombic phase and a monoclinic phase, similar to those in the LTZSO sample at ambient pressure (Figure 1a), while the $LaTaTiO_6$ sample consists of a single orthorhombic phase, similar to that in the LTTSO sample at ambient pressure (Figure 1b).

The UV−vis absorption spectra of the $LaTaO_4$ and $LaTaTiO_6$ samples are shown in Figure S1b. Their first onset absorption edges give band gaps of 4.0 and 3.1 eV for $LaTaO_4$ and $LaTaTiO_6$, respectively.

Table 2 lists the band gap data derived from this work and those from the literature for several oxysulfides and oxides of interest at ambient conditions. It is seen from Table 2 that, at ambient pressure, the band gaps of the oxysulfides $La_2Ta_2ZrS_2O_8$ (∼2.4 eV) and $La_2Ta_2TiS_2O_8$ (∼1.8 eV)[10] are at least ∼1 eV lower than those of the corresponding two oxides $LaTiO_4$ (∼3.4−4.0 eV) and $LaTaTiO_6$ (∼2.9−3.4 eV). Thus, under UV−vis illumination, the UV−vis adsorption of the LTZSO and LTTSO samples (mixed phases) should be determined primarily by the $La_2Ta_2ZrS_2O_8$ phase and the $La_2Ta_2TiS_2O_8$ phase, respectively. Thus, the band gaps (2.3 and 1.8 eV) derived from the LTZSO and LTTSO samples (Figure 1c) represent those of the oxysulfide phases of $La_2Ta_2ZrS_2O_8$ and $La_2Ta_2TiS_2O_8$, respectively. These values are in good agreement with those reported in ref 10 (see Table 2).

3.2. Structural Evolution of Oxysulfides at High Pressure.

Figure 2a,b shows synchrotron HP-XRD patterns of the LTZSO and LTTSO samples. At high pressure, all diffraction peaks shift to higher angles due to compression of interplanar distances. For the LTZSO sample (Figure 1a), there is a pressure-induced phase transition above ∼22.6 GPa, as evidenced by the appearances of several new diffraction peaks and concurrent weakening or even disappearances of several original diffraction peaks. Similarly, there is a high-pressure phase transition at ∼24.6 GPa in the LTTSO sample (Figure 1b). For both samples, upon decompression to 0.1 or 0.2 GPa, the diffraction patterns (topmost curves) revert to those before starting compression (bottom-most curves), indicating that these phase transitions are reversible. The mixed nature of both the synthesized oxysulfide samples prevented the identification of the new phases based on the available HP-XRD data. However, combining the HP-XRD data with the HP-Raman spectroscopy data (Figure S2), we infer that the high-pressure phase transition of the LTZSO sample at ∼22.6 GPa is from the $La_2Ta_2ZrS_2O_8$ phase and the one of the LTTSO samples at ∼24.6 GPa is from the $La_2Ta_2TiS_2O_8$ phase (see the SI).

We carried out Rietveld fitting of the XRD patterns shown in Figure 2a,b before the phase transitions, i.e., at $P < \sim 23$ and ∼25 GPa for the LTZSO and LTTSO samples, respectively. Representative fittings are shown in Figure S3a,b; the derived unit-cell volume and lattice parameters as a function of the pressure of the $La_2Ta_2ZrS_2O_8$ and $La_2Ta_2TiS_2O_8$ phases are shown in Figure 2c,d and those of the $LaTaO_4$ and $LaTaTiO_6$ phases are shown in Figure S3c−f.

We fitted the *P*−*V* data points of the $La_2Ta_2ZrS_2O_8$ and $La_2Ta_2TiS_2O_8$ phases using a third-order Birch−Murnaghan equation of state (EOS),[20] as shown in Figure 2c.

$$P(V) = 1.5B_0\left[\left(\frac{V_0}{V}\right)^{7/3} - \left(\frac{V_0}{V}\right)^{5/3}\right] \times \left\{1 + \frac{3}{4}(B_0' - 4) \times \left[\left(\frac{V_0}{V}\right)^{3/2} - 1\right]\right\} \quad (1)$$

where *P* is the pressure, B_0 is the bulk modulus, B_0' is the pressure derivation of the bulk modulus, and V_0 and *V* are the unit-cell volume at ambient pressure and pressure *P*, respectively. From the fittings, we obtain $B_0 = 122.5 \pm 7.1$ GPa at fixed $B_0' = 4$[21] for $La_2Ta_2ZrS_2O_8$ and $B_0 = 132.6 \pm 5.7$

Table 2. Structures and Properties of the Relevant Oxysulfide/Oxide Compounds at Ambient Pressure

compound	structure	space group	density (g/cm^3)	band gap (eV)	notes and ref
$La_2Ta_2ZrS_2O_8$	orthorhombic	*Pnnm*		2.4	UV−vis[10]
				2.3	Figure 1c, this work
$La_2Ta_2TiS_2O_8$	orthorhombic	*Pnnm*		1.8	UV−vis[10]
				1.8	Figure 1c, this work
$LaTiO_4$	monoclinic	$P2_1/c$	7.608	3.444	Rec. #mp-4421[17]
$LaTiO_4$	orthorhombic	$Cmc2_1$	7.553	3.39	Rec. #mp-3998[17]
$LaTiO_4$				3.8	UV−vis[18]
				4.0	Figure S1b, this work
$LaTiO_4$	monoclinic			3.75	UV−vis[19]
$LaTaTiO_6$	orthorhombic	$Pna2_1$	6.646	2.929	Rec. #mp-1222878[17]
		Pnma		3.1	Figure S1b, this work
$LaTaTiO_6$	monoclinic	*C*2	6.343	3.362	Rec. #mp-1222764[17]

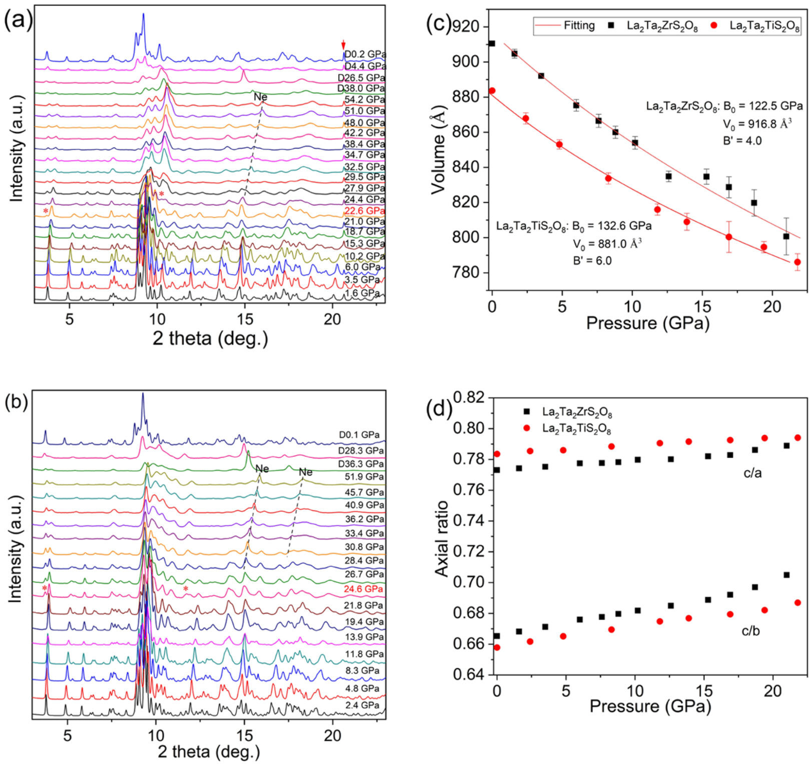

Figure 2. HP-XRD patterns of the LTZSO sample (a) and the LTTSO sample (b) (X-ray wavelength 0.4959 Å), as well as the pressure dependences of the unit-cell volumes (c) and the axial ratios (d) of the $La_2Ta_2ZrS_2O_8$ and $La_2Ta_2TiS_2O_8$ phases. In (a, b), peaks marked by "*" are from emerging new high-pressure phases. Peaks labeled by "Ne" are from the pressure medium Ne. The peaks pointed by the red arrow at ∼20.7° in (a) are from an unknown source in the measurement system as they do not shift with the pressure. The solid lines in (c) are the fits to the third-order Birch−Murnaghan equation of state.

GPa at fixed $B_0' = 6$ for $La_2Ta_2TiS_2O_8$ ($B_0' = 6$ was determined such that the EOS fitting could yield lower deviations from the data than at $B_0' = 4$). The larger B_0 and B_0' of $La_2Ta_2TiS_2O_8$ than those of $La_2Ta_2ZrS_2O_8$ indicate that the former has a more rigid framework at high pressure than the latter.

3.3. Electrical Resistances at High Pressure.

Figures S4 and S5 show the in situ high-pressure AC-impedance spectra of the LTZSO and LTTSO samples, respectively, in the form of the Nyquist plot.[22] As shown previously,[23] under AC polarization, charge carriers in grains (particles) of a conducting material experience two concurrent electrical-transport processes—one in the grain interiors (bulk) and another in the grain boundaries. These processes produce two joint semicircles in the Nyquist plot: a left semicircle (or arc) in the low-impedance region representing the bulk electrical conduction and a right one in the high-impedance region corresponding to the grain boundary electrical conduction. The diameter of the semicircle (or arc) equals the electrical resistance of the corresponding transport process of the charge carriers. If the overall carrier transport is dominated by the bulk conduction, only the left semicircle (arc) is formed, as seen in the spectra of the LTZSO and LTTSO samples (Figures S4 and S5) in this work.

Figures S4 and S5 show that the semicircle diameters of the Nyquist plots of the two samples change significantly with pressure, indicating strong pressure dependences of their electrical-transport properties. We designed two equivalent circuits (Figure S6) that could fit the AC-impedance spectra of the two samples quite well. Representative fittings (using the ZView software) are illustrated in Figure S6. From the fittings,

https://dx.doi.org/10.1021/acs.jpcc.0c03231
J. Phys. Chem. C 2020, 124, 14477−14484

the pressure-dependent electrical resistances of the LTZSO and LTTSO samples are depicted in Figure 3.

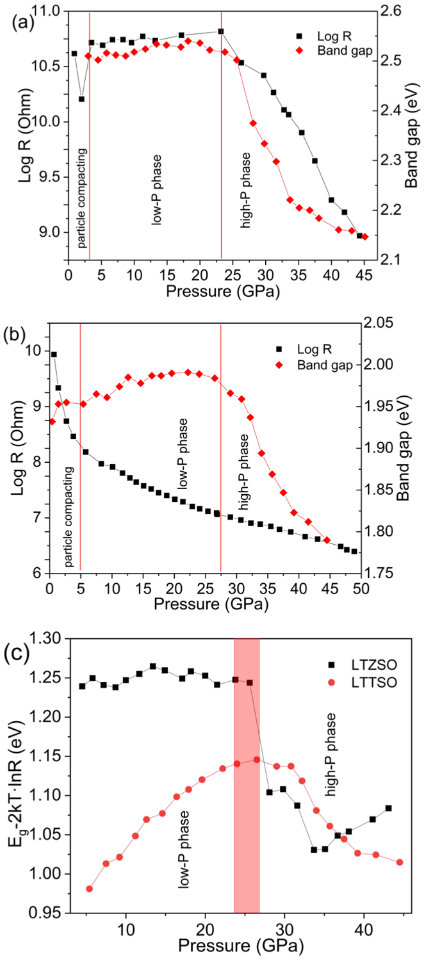

Figure 3. Pressure dependences of the log(resistance) and band gaps of the LTZSO sample (a) and the LTTSO sample (b) under compression. (c) $E_g - 2kT\ln(R(\Omega))$ as a function of pressure for the two samples.

The pressure dependence of the resistance of the LTZSO sample (Figure 3a) can be roughly classified into three regions. First, at $P < \sim 3$ GPa, the resistance decreases with the increasing pressure due to particle compacting under compression, which forms intimate contacts among sample grains.[23] Second, the resistance exhibits a slightly increasing trend with pressure between ~3 and 23 GPa. Third, in P from ~23 to 46 GPa, the resistance decreases sharply with the increasing pressure. The drastic drop in the resistance at ~23 GPa coincides with a fast decrease in the band gap (see below) that can be attributed to a phase transition from the orthorhombic $La_2Ta_2ZrS_2O_8$ phase to a high-pressure phase (see above).

Similarly, the fast decrease in the resistance of the LTTSO sample from ambient pressure to ~5 GPa (Figure 3b) arises from the particle compacting under compression. In ~5−50 GPa, the resistance decreases steadily with the increasing pressure. Although the pressure-dependent band gap (see below) of the LTTSO sample (Figure 3b) exhibits a marked drop at ~25 GPa, which can also be attributed to the high-pressure phase transition from the orthorhombic $La_2Ta_2TiS_2O_8$ phase to a high-pressure phase (see above), the pressure dependence of the resistance shows a trend different from that of the LTZSO sample (Figure 3a). Such a difference in the two samples can be sourced to their different responses in the carrier mobility under compression, as discussed below.

In a semiconductor, either or both of the electron and hole can act as the charge carrier. The electrical conductivity (σ) of the semiconductor is proportional to the carrier mobility (μ) and the carrier concentration (c)[24]

$$\sigma = ec\mu \tag{2}$$

where e is the magnitude of the charge of an electron. For an intrinsic semiconductor, part of the valence electrons can be excited by thermal (and/or photon) energy to reach the conduction bands, leaving equal amounts of holes in the valence bands. The generated carrier concentration is proportional to $\exp(-E_g/(2kT))$,[25] where E_g is the band gap, T is the absolute temperature, and k is the Boltzmann constant. Thus, eq 2 can be written as

$$\sigma = e\mu \times L_1 \exp\left(-\frac{E_g}{2kT}\right) \tag{3}$$

where L_1 is a proportional coefficient. Then, the electrical resistance of an intrinsic semiconductor can be written as

$$R = \frac{L_2}{\sigma} = \frac{L_2}{eL_1} \times \mu^{-1} \times \exp\left(\frac{E_g}{2kT}\right)$$

or

$$R = L\mu^{-1} \times \exp\left(\frac{E_g}{2kT}\right) \tag{4}$$

where L_2 is a geometric constant of the conductor and $L = (L_2/(eL_1))$ is a coefficient presumed to be independent of the pressure. Equation 4 can be transformed into the following form

$$2kT \ln\left(\frac{\mu}{L}\right) = E_g - 2kT \ln R \tag{5}$$

Thus, if the pressure dependences of the band gap and the resistance of a semiconductor are known, the pressure dependence of the carrier mobility can be deduced in terms of eq 5.

To obtain the pressure-dependent band gaps of the LTZSO and LTTSO samples, we measured their UV−vis absorption spectra at high pressure. Then, the Tauc−Mott plots[26,27] of the UV−vis absorption data (see the representative plots in Figure S7) were used to estimate the band gaps of the samples. In a Tauc−Mott plot, the cross point between a linear regression line and the baseline determines the band gap energy.[10] The derived band gaps of the LTZSO and LTTSO samples as a function of pressure are shown in Figure 3a,b. Then, the $E_g - 2kT\ln R$ was calculated as a function of pressure, as illustrated in Figure 3c (in the calculations, E_g and $\ln R$ were aligned at the same pressures via numerical interpolation).

As discussed above, the UV−vis absorptions of the LTZSO and LTTSO samples are determined by the oxysulfide phases rather than the oxide phases. Thus, the high-pressure band gaps derived from the Tauc−Mott plots are actually those of the two oxysulfides $La_2Ta_2ZrS_2O_8$ and $La_2Ta_2ZrS_2O_8$. Again, as the band gaps of the two oxides are at least ~1 eV higher than those of the oxysulfides (Table 2), the carrier concentrations produced from the impurity oxides would be ~exp(−1.0/(2kT)) ~4 × 10^{-9} times those of the two oxysulfides and thus the electrical resistances of the oxide grains should be much higher than those of the oxysulfides. Even though the impurities can scatter the electrons and phonons in the mixtures, with increasing pressure, the contacts between oxysulfide grains become tighter and hence the electrical transports in the LTZSO and LTTSO samples should be determined mostly by the oxysulfide phases $La_2Ta_2ZrS_2O_8$ and $La_2Ta_2TiS_2O_8$. Therefore, the measured electrical resistances, band gaps, and the deduced $E_g - 2kT\ln(R)$ values in Figure 3 are pertinent only to the two oxysulfide phases rather than the two oxide phases.

Figure 3c shows that before the high-pressure phase transitions in the $La_2Ta_2ZrS_2O_8$ and the $La_2Ta_2TiS_2O_8$ phases at ~23−27 GPa, the carrier mobility stays almost unchanged in the former, while it increases quickly with pressure in the latter. After the phase transitions, the carrier mobilities of the new high-pressure phases decrease quickly with the pressure (with a subsequent increase in the LTZSO sample at high pressure). Many factors can affect the carrier mobility, predominantly the optical phonon scattering[25] for an intrinsic semiconductor at room temperature.[28] In this case, the carrier mobility due to the phonon scattering is inversely proportional to the phonon density and carrier thermal velocity[25]

$$\mu_{\text{phonon}} \propto \frac{1}{\text{phonon density} \times \text{carrier thermal velocity}}$$

At atmospheric pressure, the temperature dependence of the carrier mobility can be described by the following empirical formula[28]

$$\mu_{\text{phonon}} \propto T^{-n} \quad \text{with } 1.5 < n < 2.5$$

However, there is no known analytical description of the pressure dependence of the carrier mobility. Using the Debye model of lattice vibration (see, e.g., ref 24), we assume that the phonon density is proportional to the Debye frequency (ω_D) and hence the Debye temperature θ_D, which is roughly proportional to the square root of the bulk modulus (B).[29] Then, if we treat the carrier thermal motion as being similar to a gas molecule diffusion, the carrier thermal velocity will be inversely proportional to pressure.[30] Putting these relationships together, we obtain

$$\begin{aligned}\mu_{\text{phonon}} &\propto \frac{1}{\text{phonon density} \times \text{carrier thermal velocity}}\\ &\propto \frac{1}{\theta_D/P}\end{aligned}$$

$$\mu_{\text{phonon}} \propto \frac{1}{B^{1/2}/P} \propto (B_0 + B_0'P)^{-1/2}P \tag{6}$$

Thus, using the determined EOS parameters of the two oxysulfide orthorhombic phases (see above), we obtain

$$\mu_{\text{phonon}} \propto (122.5 + 4P)^{-1/2}P$$
$$\text{for the } La_2Ta_2ZrS_2O_8 \text{ phase, and}$$

$$\mu_{\text{phonon}} \propto (132.6 + 6P)^{-1/2}P$$
$$\text{for the } La_2Ta_2TiS_2O_8 \text{ phase}$$

These relationships predict that before the high-pressure phase transitions, the carrier mobility of the orthorhombic $La_2Ta_2ZrS_2O_8$ phase is higher than that of the $La_2Ta_2TiS_2O_8$ phase, and their mobilities increase with increasing pressure. This is basically consistent with the experimentally derived results (Figure 3c) except that the carrier mobility of the $La_2Ta_2ZrS_2O_8$ phase is less sensitive to pressure. After the high-pressure phase transitions at ~23−27 GPa, the carrier mobilities of the two new high-pressure phases decrease dramatically (Figure 3c). This can be attributed to the increased bulk moduli of the high-pressure phases due to the increased mass densities and other factors such as that the electron−electron scattering plays a role.

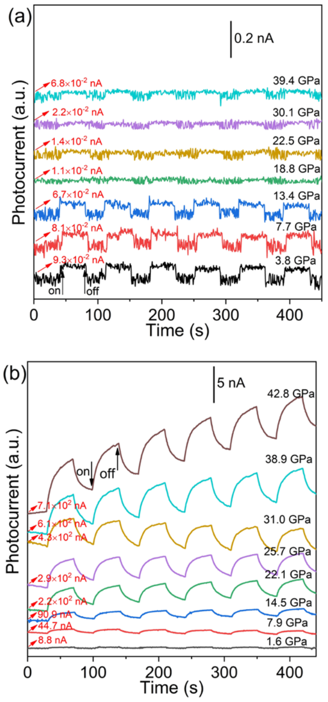

Figure 4. Photocurrents of the LTZSO sample (a) and the LTTSO sample (b) under compression. The dark current before the first application of a UV illumination is indicated by a red arrow in each curve. The "on" and "off" indicate the start and the end of a UV illumination pulse in a series of repeated tests.

3.4. Photocurrents at High Pressure.

Figure 4 shows the measured electrical currents flowing through an LTZSO or an LTTSO sample under an electrical polarization of a 3 V DC voltage. The currents were measured with and without application of a pulse of UV illumination on the sample while under compression in a DAC. No ambient photocurrents were obtained because a nonzero initial pressure has to be applied to the sample in assembling the DAC set. The results show that without the UV illumination, the variations of the dark currents (the readings pointed by the red arrows in the diagrams) with pressure are consistent with the pressure dependences of the resistances of the two samples (Figure 3a,b). That is, the dark current of a sample equals approximately the quotient of the voltage (3 V) divided by the resistance. However, they show quite different responses to the UV illumination as the pressure increases: the photocurrent (the jump in the current from the dark current baseline) of the LTZSO sample decreases with increasing P and then almost disappears at $P \geq 18.8$ GPa (Figure 4a), while that of the LTTSO sample increases continuously with increasing *P* and is most obvious at the maximum pressure of 42.8 GPa (Figure 4b). The former phenomenon (Figure 4a) is counterintuitive and may be related to the creation of defects in the crystal at high pressure, which annihilates the photons and hence prevent the production of photocurrents. The latter phenomenon (Figure 4b) aligns well with the pressure dependence of the resistance of the LTTSO sample (Figure 3b), i.e., the UV illumination produces abundant photoelectron, whose flow is regulated by Ohm's law.

4. CONCLUSIONS

Two oxysulfide compounds, $La_2Ta_2ZrS_2O_8$ and $La_2Ta_2TiS_2O_8$, were synthesized via solid-state reactions at high temperatures. High-pressure XRD and Raman spectroscopy data reveal that, under compression, the orthorhombic phases of $La_2Ta_2ZrS_2O_8$ and $La_2Ta_2TiS_2O_8$ transform into two new high-pressure phases at ~23 and 25 GPa, respectively. Although the pressure dependences of the band gaps of the two phases are similar, there are striking differences in the pressure dependences of their electrical resistances due to their different behaviors in the carrier mobility while under compression: the resistance of $La_2Ta_2ZrS_2O_8$ shows a marked drop at the phase transition, while that of $La_2Ta_2TiS_2O_8$ exhibits a steady decrease with increasing pressure. Moreover, depending on the magnitude of pressure, the resistance of $La_2Ta_2ZrS_2O_8$ is about a hundred to a thousand-fold higher than that of $La_2Ta_2TiS_2O_8$ when they are of similar sample sizes. Under compression, the $La_2Ta_2TiS_2O_8$ compound produces much higher photocurrents than $La_2Ta_2ZrS_2O_8$, suggesting that the former is a better candidate than the latter for applications in photocatalysis, photovoltaics, photoelectric devices, etc.

■ ASSOCIATED CONTENT

Supporting Information

The Supporting Information is available free of charge at https://pubs.acs.org/doi/10.1021/acs.jpcc.0c03231.

> Syntheses and characterizations of $LaTaO_4$ and $LaTaTiO_6$, high-pressure Raman spectra, Rietveld fittings of high-pressure XRD data, high-pressure AC-impedance spectra, high-pressure UV−vis absorption spectra (PDF)

■ AUTHOR INFORMATION

Corresponding Author

Hengzhong Zhang − *Center for High Pressure Science and Technology Advanced Research, Shanghai 201203, China;* orcid.org/0000-0003-2322-2274; Phone: +86-21-80177095; Email: hengzhong.zhang@hpstar.ac.cn

Authors

Junxiu Liu − *Center for High Pressure Science and Technology Advanced Research, Shanghai 201203, China*
Jian Chen − *Center for High Pressure Science and Technology Advanced Research, Shanghai 201203, China*
Weiwei Li − *Center for High Pressure Science and Technology Advanced Research, Shanghai 201203, China*
Hua Tian − *Center for High Pressure Science and Technology Advanced Research, Shanghai 201203, China*
Xiaoliang Zhang − *Center for High Pressure Science and Technology Advanced Research, Shanghai 201203, China*
Nana Li − *Center for High Pressure Science and Technology Advanced Research, Shanghai 201203, China*
Jinyuan Yan − *Advanced Light Source, Lawrence Berkeley National Laboratory, Berkeley, California 94720, United States*
Martin Kunz − *Advanced Light Source, Lawrence Berkeley National Laboratory, Berkeley, California 94720, United States*
Bin Chen − *Center for High Pressure Science and Technology Advanced Research, Shanghai 201203, China*

Complete contact information is available at: https://pubs.acs.org/10.1021/acs.jpcc.0c03231

Notes

The authors declare no competing financial interest.

■ ACKNOWLEDGMENTS

This work was supported by the National Natural Science Foundation of China (grant no. 21875005). The research used the resources of the Advanced Light Source (ALS), Berkeley, California. ALS is a US DOE Office of Science User Facility under contract no. DE-AC02-05CH11231. The high-pressure synchrotron X-ray diffraction was conducted at the high-energy beamline station 12.2.2 of the Advanced Light Source, Berkeley, California. We thank Renshu Wang for help with sample preparations.

■ REFERENCES

(1) Hisatomi, T.; Kubota, J.; Domen, K. Recent Advances in Semiconductors for Photocatalytic and Photoelectrochemical Water Splitting. *Chem. Soc. Rev.* **2014**, *43*, 7520−7535.

(2) Fujishima, A.; Honda, K. Electrochemical Photolysis of Water at a Semiconductor Electrode. *Nature* **1972**, *238*, 37−38.

(3) Kudo, A.; Miseki, Y. Heterogeneous Photocatalyst Materials for Water Splitting. *Chem. Soc. Rev.* **2009**, *38*, 253−278.

(4) Domen, K.; Kudo, A.; Onishi, T. Mechanism of Photocatalytic Decomposition of Water into H_2 and O_2 over NiO-$SrTiO_3$. *J. Catal.* **1986**, *102*, 92−98.

(5) Yamakata, A.; Ishibashi, T. A.; Kato, H.; Kudo, A.; Onishi, H. Photodynamics of $NaTaO_3$ Catalysts for Efficient Water Splitting. *J. Phys. Chem. B* **2003**, *107*, 14383−14387.

(6) Takata, T.; Furumi, Y.; Shinohara, K.; Tanaka, A.; Hara, M.; Kondo, J. N.; Domen, K. Photocatalytic Decomposition of Water on Spontaneously Hydrated Layered Perovskites. *Chem. Mater.* **1997**, *9*, 1063−1064.

(7) Osterloh, F. E. Inorganic Materials as Catalysts for Photochemical Splitting of Water. *Chem. Mater.* **2008**, *20*, 35−54.

(8) Ishikawa, A.; Takata, T.; Kondo, J. N.; Hara, M.; Kobayashi, H.; Domen, K. $Sm_2Ti_2S_2O_5$ as a Stable Photocatalyst for Water Oxidation and Reduction under Visible Light Irradiation ($\lambda \leq 650$ nm). *J. Am. Chem. Soc.* **2002**, *124*, 13547−13553.

(9) Cario, L.; Kabbour, H.; Guillot-Deudon, C.; Meerschaut, A. A Mixed-Valent Niobium Oxysulfide, $La_2Nb_3S_2O_8$. *Acta Crystallogr., Sect. C: Cryst. Struct. Commun.* **2003**, *59*, i55−i56.

(10) Goto, Y.; Seo, J.; Kumamoto, K.; Hisatomi, T.; Mizuguchi, Y.; Kamihara, Y.; Katayama, M.; Minegishi, T.; Domen, K. Crystal Structure, Electronic Structure, and Photocatalytic Activity of Oxysulfides: $La_2Ta_2ZrS_2O_8$, $La_2Ta_2TiS_2O_8$, and $La_2Nb_2TiS_2O_8$. *Inorg. Chem.* **2016**, *55*, 3674−3679.

(11) Mao, H. K.; Chen, B.; Chen, J.; Li, K.; Lin, J. F.; Yang, W.; Zheng, H. Recent Advances in High-Pressure Science and Technology. *Matter Radiat. Extremes* **2016**, *1*, 59−75.

(12) Kunz, M.; MacDowell, A. A.; Caldwell, W. A.; Cambie, D.; Celestre, R. S.; Domning, E. E.; Duarte, R. M.; Gleason, A. E.; Glossinger, J. M.; Kelez, N.; et al. A Beamline for High-Pressure Studies at the Advanced Light Source with a Superconducting Bending Magnet as the Source. *J. Synchrotron Radiat.* **2005**, *12*, 650−658.

(13) Mao, H. Design and Varieties of the Megabar Cell. *Year Book - Carnegie Inst. Washington* **1978**, *77*, 904−908.

(14) Toby, B. H. Expgui, a Graphical User Interface for GSAS. *J. Appl. Crystallogr.* **2001**, *34*, 210−213.

(15) Hellenbrandt, M. The Inorganic Crystal Structure Database (ICDS)—Present and Future. *Crystallogr. Rev.* **2004**, *10*, 17−22.

(16) Gražulis, S.; Daškevič, A.; Merkys, A.; Chateigner, D.; Lutterotti, L.; Quiros, M.; Serebryanaya, N. R.; Moeck, P.; Downs, R. T.; Le Bail, A. Crystallography Open Database (COD): An Open-Access Collection of Crystal Structures and Platform for World-Wide Collaboration. *Nucleic Acids Res.* **2012**, *40*, D420−D427.

(17) Jain, A.; Ong, S. P.; Hautier, G.; Chen, W.; Richards, W. D.; Dacek, S.; Cholia, S.; Gunter, D.; Skinner, D.; Ceder, G.; Persson, K. A. Commentary: The Materials Project: A Materials Genome Approach to Accelerating Materials Innovation. *APL Mater.* **2013**, *1*, No. 011002.

(18) Meiying, L.; Wansheng, Y.; Zhibin, L.; Takata, T.; Domen, K.; Can, L. Photocatalytic Water Splitting to Hydrogen over a Visible Light-Driven $LaTaON_2$ Catalyst. *Chin. J. Catal.* **2006**, *27*, 556−558.

(19) Machida, M.; Murakami, S.; Kijima, T.; Matsushima, S.; Arai, M. Photocatalytic Property and Electronic Structure of Lanthanide Tantalates, $LnTaO_4$ (Ln = La, Ce, Pr, Nd, and Sm). *J. Phys. Chem. B* **2001**, *105*, 3289−3294.

(20) Birch, F. Finite Strain Isotherm and Velocities for Single-Crystal and Polycrystalline Nacl at High Pressures and 300 K. *J. Geophys. Res.* **1978**, *83*, 1257−1268.

(21) Mitra, S. *High Pressure Geochemistry & Mineral Physics: Basics for Planetology and Geo-Material Science*; Elsevier: Amsterdam, Boston, 2004.

(22) Sinclair, D. C.; West, A. R. Impedance and Modulus Spectroscopy of Semiconducting $BaTiO_3$ Showing Positive Temperature Coefficient of Resistance. *J. Appl. Phys.* **1989**, *66*, 3850−3856.

(23) Liu, J.; Yan, J.; Shi, Q.; Dong, H.; Zhang, J.; Wang, Z.; Huang, W.; Chen, B.; Zhang, H. Pressure Dependence of Electrical Conductivity of Black Titania Hydrogenated at Different Temperatures. *J. Phys. Chem. C* **2019**, *123*, 4094−4102.

(24) Naumann, R. J. *Introduction to the Physics and Chemistry of Materials*; CRC Press: Boca Raton, 2008.

(25) Hu, C. *Modern Semiconductor Devices for Integrated Circuits*; Prentice Hall: Upper Saddle River, NJ, 2010; Vol. *1*.

(26) Davis, E.; Mott, N. Conduction in Non-Crystalline Systems V. Conductivity, Optical Absorption and Photoconductivity in Amorphous Semiconductors. *Philos. Mag.* **1970**, *22*, 0903−0922.

(27) Sayed, F. N.; Polshettiwar, V. Facile and Sustainable Synthesis of Shaped Iron Oxide Nanoparticles: Effect of Iron Precursor Salts on the Shapes of Iron Oxides. *Sci. Rep.* **2015**, *5*, No. 9733.

(28) Li, S. S. Metal−Semiconductor Contacts. In *Semiconductor Physical Electronics*, 2nd ed.; Springer: New York, 2006.

(29) Siethoff, H.; Ahlborn, K. Debye-Temperature-Elastic-Constants Relationship for Materials with Hexagonal and Tetragonal Symmetry. *J. Appl. Phys.* **1996**, *79*, 2968−2974.

(30) Cussler, E. L. *Diffusion: Mass Transfer in Fluid Systems*, 3rd ed.; Cambridge University Press: Cambridge; New York, 2009.